University Library

MINERVA ACCESS

A gateway to Melbourne's research publications

Minerva Access is the Institutional Repository of The University of Melbourne

Author/s:
Meng, J;Cadusch, JJ;Crozier, KB

Title:
Detector-Only Spectrometer Based on Structurally Colored Silicon Nanowires and a Reconstruction Algorithm

Date:
2020-01-08

Citation:
Meng, J., Cadusch, J. J. & Crozier, K. B. (2020). Detector-Only Spectrometer Based on Structurally Colored Silicon Nanowires and a Reconstruction Algorithm. NANO LETTERS, 20 (1), pp.320-328. https://doi.org/10.1021/acs.nanolett.9b03862.

Persistent Link:
https://hdl.handle.net/11343/240499

Detector-only spectrometer based on structurally-colored silicon nanowires and a reconstruction algorithm

Jiajun Meng[§*], *Jasper J. Cadusch*[§], *and Kenneth B. Crozier*[§, ¶*].

§ Department of Electrical and Electronic Engineering, The University of Melbourne, Victoria 3010, Australia.

¶ School of Physics, The University of Melbourne, Victoria 3010, Australia.

KEYWORDS: microspectrometers, silicon nanowires, photodetectors, nanofabrication,

ABSTRACT

Spectroscopy is a cornerstone of the field of optics. Conventional spectrometers generally require two elements. The first provides wavelength selectivity, e.g. diffraction grating or Michelson interferometer. The second is a detector (or detector array). Many applications would benefit from very small and lightweight spectrometers. This motivates us to investigate what may be regarded as an ultimate level of miniaturization for a spectrometer, in which it consists solely of a detector array. We demonstrate a chip containing 24 pixels, each comprising a silicon nanowire (Si NW) array photodetector formed above a planar photodetector. The NWs are structurally-colored,

enabling us to engineer the responsivity spectra of all photodetectors in the chip. Each pixel thus combines wavelength selectivity and photodetection functions. We demonstrate the use of our chip to reconstruct the spectrum of an unknown light source impinging upon it. This is achieved by an algorithm that takes as its inputs the measured photocurrents from the pixels and a library of their responsivity spectra.

INTRODUCTION

Spectrometers are a workhorse tool of optics, with applications ranging from basic scientific research to industrial process monitoring, remote sensing and medical diagnostics. Spectrometers generally contain a wavelength-selective element and an element that performs photodetection. At visible wavelengths, this is frequently achieved by combining a diffraction grating[1] with a photodetector array. In the mid- to long-wave infrared, the usual approach is to combine a Michelson interferometer with a single photodetector, e.g. in the Fourier transform infrared spectrometer (FTIR)[1]. For most current applications, this approach works well. However, at the time of writing there is a growing trend toward the miniaturization of optical systems, to enable their inclusion in platforms that include smartphones, cars, and lightweight drones. For some emerging applications, high spectral resolution is less important than the size, weight and cost of the system. This motivates the development of compact spectrometers based on silicon microfabrication. In one approach, a photodetector array is paired with an array of filters. For the latter, thin films[2, 3], colloidal quantum dots[4] and plasmonic nanostructures[5, 6] have been employed. In another approach, miniature spectrometers are realized using microelectromechanical systems (MEMS) fabrication methods[7-9]. In both methods, different structures are employed for spectral filtering and photodetection. This motivates us to investigate whether these functions can be

combined into a single structure, namely a photodetector with an engineered responsivity, and to realize a compact spectrometer using an array of pixels containing such photodetectors in conjunction with an algorithm. That is the topic of this paper.

It has been long known that plants and animals can exhibit vivid colors that arise from structural effects rather than from other mechanisms such a pigments[10]. This is known as structural color. In recent years, there has been much interest in structurally coloring surfaces using plasmonic materials[11-13] and high index semiconductors[14-19]. This has been largely pursued for potential applications such as optical document security and displays, but also as photodetectors. Various forms of imaging, including color[20] and polarization-resolved[21], have been demonstrated using the latter. These have made use of the fact that semiconductor nanowires act as nanoscale optical waveguides, and thus have absorption spectra with peaks whose positions can be tuned by varying the nanowire radius[14, 15]. To the best of our knowledge, however, the experimental realization of a spectrometer based on structurally-colored nanowires has not been previously reported. Here, we demonstrate such a chip. Our chip contains 24 pixels, each consisting of a photodetector comprising vertically-oriented silicon nanowires (doped p+/i(n-)/n+) formed above a planar photodetector (doped n+/i(n-)/p+). We demonstrate spectral reconstruction at visible wavelengths using this chip. The organization of this paper is as follows. We begin by describing the fabrication process. We then discuss the optical response using the results of electromagnetic simulations. We next discuss the optical characterization of fabricated devices and compare the results to the predictions of simulations. We then demonstrate that our device can be used as a spectrometer. This includes a discussion of the reconstruction algorithms we employ, the recursive least squares

method and lasso regression. We conclude this paper with a summary of key results and a discussion of future work.

METHODS

We illustrate our nanowire spectrometer chip schematically in Fig. 1a and 1b. As depicted in Fig. 1a, the 24 pixels of the spectrometer appear different colors. This is because each pixel contains a periodic array of nanowires of a certain radius. This results in it absorbing certain wavelengths more strongly than others. We have discussed this mechanism in previous work[15, 20]. In addition to this leading to the pixels appearing different colors, this phenomenon also results in the photodetectors they contain having distinct responsivity spectra. It is the latter that allows the chip to function as a spectrometer. While other methods exist for tailoring the responsivities of photodetectors for spectral reconstruction (e.g. Ref [22]), the nanowire geometry is particularly compelling due to the large body of work that exists on bottom-up[23] and top-down[24] methods for fabricating nanowires, and their incorporation into a variety of devices[25, 26]. We note that recent work has shown that the compositional grading of a single nanowire allows it to function as a spectrometer[27]. This further illustrates the possibilities available with nanowires, though we argue that from a manufacturing standpoint, achieving wavelength selectivity by controlling the nanowire radius (i.e. this work) is more readily accomplished than doing so by varying composition in a precise manner with axial position along the nanowire (i.e. Ref [27]). We note that the responsivity spectra of both the nanowire (NW) photodetector and planar (bottom) photodetector of each pixel are modified by choice of nanowire radius. This is because the NW and planar photodetector of each pixel are arranged in a vertically-stacked configuration (Fig. 1b). The light that reaches the planar (bottom) photodetector must therefore pass through the NW

photodetector. The NWs can therefore be thought of as acting as a filter for the planar (bottom) photodetector, thereby modifying its responsivity spectrum. As illustrated in Fig. 1b, all pixels in the chip share a common contact through the p+-doped Si substrate. As illustrated schematically, biasing the top contact positive with respect to the substrate results in the nanowire and planar (bottom, or mesa) photodetectors being under forward and reverse-bias, respectively. This is also illustrated in the band diagrams that are provided in the Supporting Information. In this configuration, the change in current that results from illumination of the pixel originates from light absorbed in the planar (bottom, or mesa) photodetector. Similarly, when the voltage bias is reversed, photocurrent originates from light absorption in the nanowire photodetector. To operate the chip as a spectrometer, therefore, two photocurrents (i.e. under positive and negative biases) are measured from each of the 24 pixels, in response to the unknown light source. These currents are provided along with a library of the responsivity spectra of the photodetectors to the algorithm that performs the spectral reconstructions, i.e. estimates the spectrum of the light illuminating the chip. We note that it would also be possible to realize a spectrometer comprising only nanowire photodetectors (i.e. no mesa detectors). However, by also including mesa photodetectors, the device we demonstrate doubles the number of photocurrent measurements (while maintaining the device footprint), thereby increasing the accuracy of the spectral reconstruction.

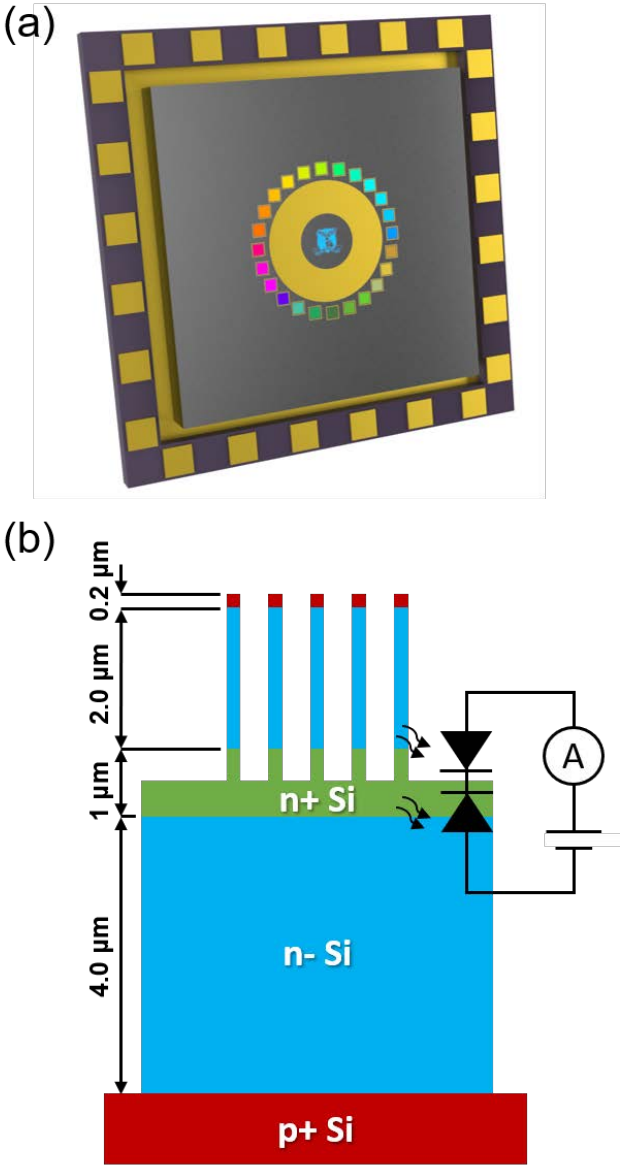


Figure 1. (a) Schematic illustration of nanowire microspectrometer, comprising 24 pixels arranged in a circular pattern. **(b).** Schematic illustration (cross sectional view) of a single pixel. Note that materials used to establish top electrical contact to each pixel are not shown in this simplified illustration. Red, green and cyan shadings indicate doping of epitaxial layers, representing p+, n+ and intrinsic (n-), respectively.

In Fig. 2a, a three-dimensional schematic illustration is provided for a single pixel after all fabrication steps are completed. Fig. 2b illustrates the three main parts of the fabrication process:

NW etching, inter-pixel isolation, and establishing electrical contacts. We describe these in greater detail in the remainder of this section.

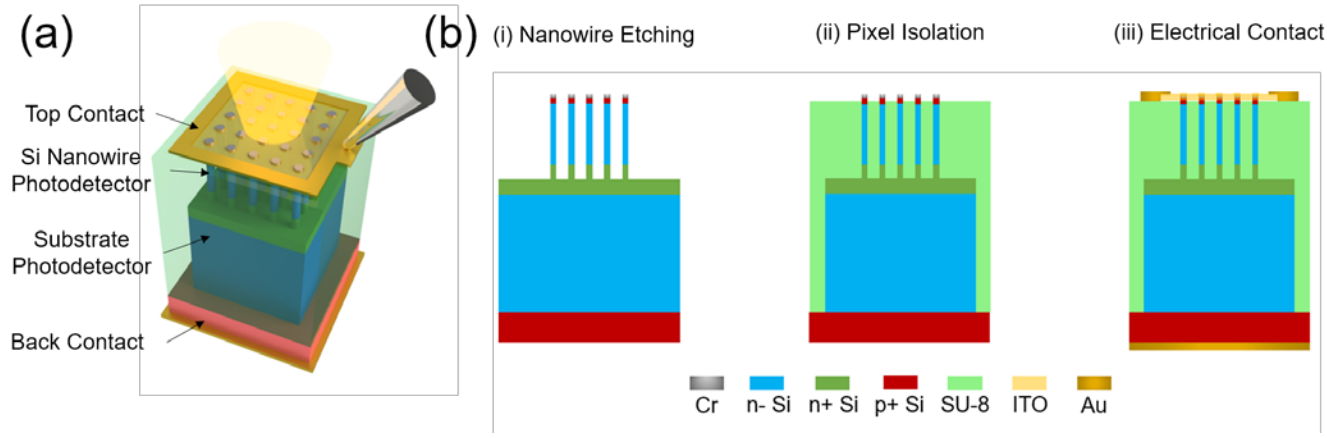


Figure 2. Device fabrication schematic. **(a)** Concept schematic of single pixel unit. **(b)** Three main stages in the fabrication flow. **(i)** nanowire etching, **(ii)** pixel isolation and planarization, **(iii)** establishment of top and bottom electrical contacts.

Fabrication starts with the preparation of the hard mask used to etch the NWs (Fig. 2b-i). The starting wafer contains multiple epitaxial layers, whose characterization by secondary ion mass spectroscopy (SIMS) was reported in Ref [28]. Polymethylmethacrylate (PMMA) is spun onto the wafer and exposed by electron beam lithography (EBL, Vistec EBPG 5000plusES) with an accelerating voltage of 100 kV. In this step, the exposed pattern consists of 24 arrays of disks (corresponding to the pixels of the chip). After development, we use electron beam evaporation (EBE, Intlvac Nanochrome II) to deposit a thin layer of chromium (40 nm thick). This is followed by a lift-off process. We next use inductively coupled plasma reactive ion etching (ICP-RIE, Oxford Instruments PLASMALAB ICP380) to etch the nanowires. The goal is to etch the NWs so that their bases are within the n+-doped layer, meaning that the height of the nanowires should be within the range of 2.2 to 3.2 μm (Fig. 1b). It is important that this etching step results in the NWs

having smooth and straight sidewalls. This ensures that they exhibit the desired waveguiding properties. We thus experiment with the parameters used in the pseudo-Bosch process used to etch the NWs. The flow rates we use for the SF_6 and C_4F_8 etch gases are 40 and 95 sccm, respectively. Scanning electron micrographs (SEMs) of etched NWs with radii of 175 nm and heights of 2.8 μm are shown in Fig 3b. Note that the metal mask (Cr, 40 nm thick) is not removed after the ICP-RIE step. This is because simulations indicate that it has little effect upon the absorption spectra of the NWs. In addition, were it to be removed using a wet etchant, there is the possibility that this process might damage the NWs. The nominal (design) radii of the NWs in the chip range from 60 to 175 nm, in steps of 5 nm. Further information on how the geometric parameters are chosen is provided in the Supporting Information. Each NW array has an extent of ~150 μm × 150 μm, comprising a square array of 188×188 nanowires with a pitch of 800 nm. The next part of the fabrication process concerns isolating the pixels from one another (Fig. 2b-ii). Optical lithography (Intelligent micropatterning SF100 XPRESS) is used to pattern a trench around each NW array. As the NWs are 2.8μm tall, we use a thick photoresist (~10 μm, AZ4562 from MicroChemicals GmbH) to ensure that they are completely covered in this step. Trenches are then etched using the same ICP-RIE process as that used to etch the NWs. The trenches are etched to a depth that exceeds 7.2 μm (measured from the tops of the NWs). Each mesa thus extends to the bottom p+ substrate. The resist is removed either by a hot acetone bath or by AZ100 remover (MicroChemicals GmbH) with ultrasonication. The SEMs of Fig 3b are taken at the conclusion of this step, i.e. after the mesas have been formed. The next step is that needed to form electrical contacts (Fig. 2b-iii). We first planarize the wafer by spinning on a thick layer (~17 μm) of the permanent epoxy SU-8 3000 (MicroChem). We choose SU-8 due to its high transmittance in the visible spectrum and its robustness to most solvents when cured. Note that we choose a circular pattern for the pixel layout

largely to mitigate against the resist being non-uniform in thickness (between the pixels) after the spin coating step. The SU-8 is cross-linked by flood UV exposure (ABM UV Flood Light Source) followed by hard baking on a hot plate. We next use ICP-RIE to etch the SU-8 for a duration sufficient to expose the p+ tips of the NWs. This is done using a combination of SF_6 (5 sccm) and oxygen (50 sccm) as the etch gases and the RIE and ICP RF power are 200 W and 500W, respectively. A typical result is shown as Fig. 3c. Over the chip, the distance by which the exposed tips protrude from the SU-8 ranges from ~200 to 300 nm. This variation results from the fact that the planarized surface is non-uniform. In addition, it is possible that there is variation in the etch rate of SU-8 from pixel to pixel. We next establish an electrical contact to each pixel. This done by forming a 185 μm ×185 μm square of the transparent conductor indium tin oxide (ITO) centered over each pixel. The ITO contacts the tops of the nanowires. This is achieved as follows. We spin photoresist on to the chip and expose it by optical lithography (Intelligent micropatterning SF100 XPRESS). After development, the ITO is deposited to a thickness of 90 nm by AC/DC sputtering (Intlvac Nanochrome). The lift-off process is then performed by immersing the sample in acetone. We next add top and back metal contacts. The top contact is added by lithography, EBE, and lift-off. The back contact is added to the back of the wafer. This is done by first dry etching the native oxide on the back of the chip with the top surface of the chip protected by a hard baked AZ4562 resist layer. We then evaporate the metal electrode by EBE and use acetone to remove the protection photoresist. In both cases, the metal is gold (Au, 200 nm thick) with chrome (50 nm thick) for adhesion. Fig. 3d shows a pixel at the conclusion of this step. The different regions of the pixel have been colored in this SEM to distinguish between the different materials they comprise. The last step of the fabrication is that of device packaging. We dice the sample into a 7.7 mm × 7.7 mm square piece using an automated wet dicing saw (Disco DAD321) and glue it

onto a dual-in-line (DIL) chip carrier using conductive carbon wire glue (Fig. 3a). We protect the front surface of the chip during the cutting process with hard-baked photoresist. This is removed after the cutting is completed. The inset of Figure 3(a) is an optical microscope image of the chip, showing all 24 pixels. It can be seen that each pixel displays its own distinctive color. An optical microscope image and an SEM image of a reference nanowire sample before stage ii is provided in the Supporting Information (Figure S2). At the center of the chip, the logo of the institution of the authors is shown. This is comprised of NWs. The uniformity of the blue regions of the logo serves as an indication of the uniformity of the NWs in these regions.

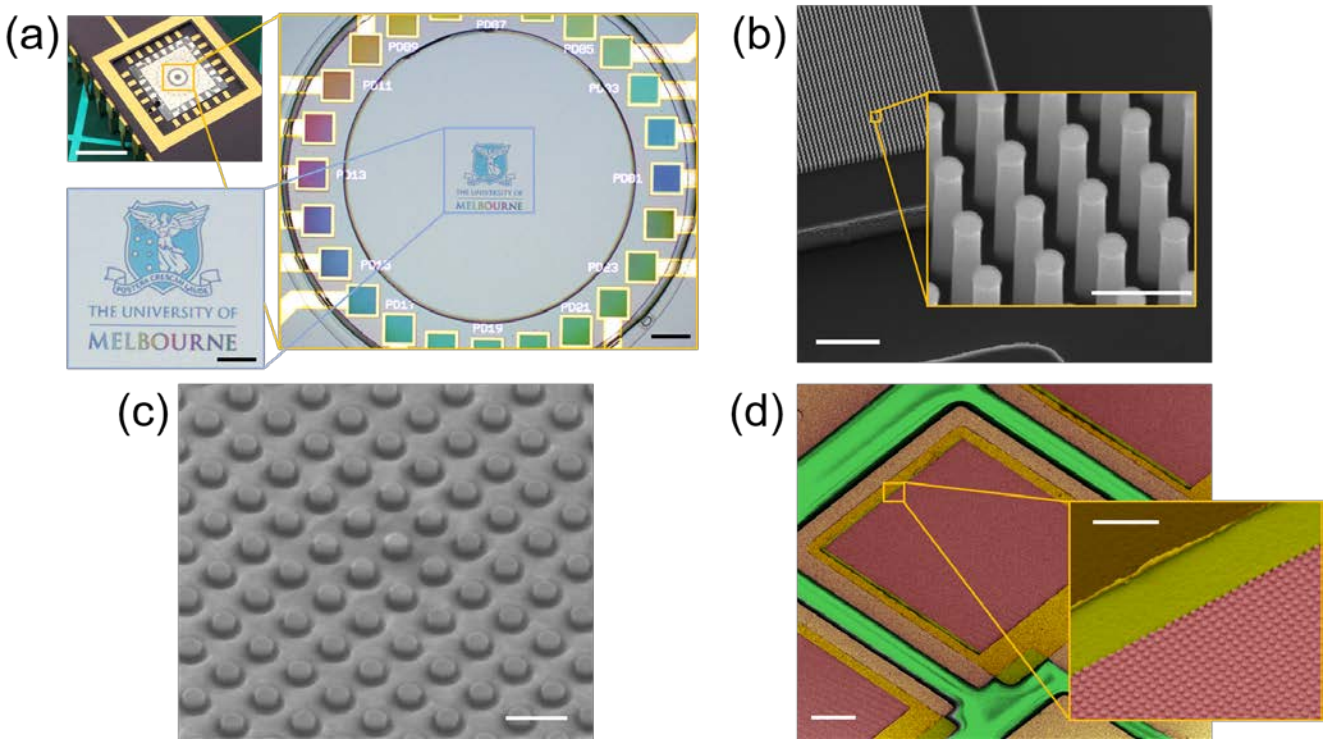


Figure 3. Device fabrication. **(a)** Photograph of device mounted in DIL-24 chip carrier, with 5 mm scale bar. Inset shows bright field optical microscope image of center of device, with 200 μm scale bar. Logo of institution of authors is realized in center of chip, using nanowires of different radii. Blue regions of goddess figure and words “The University of” are realized using NWs with nominal radii of 60 nm. Multicolored font used for word “MELBOURNE” are realized with NWs that vary in radius from 60 to 175 nm. Bottom left inset scale bar is 100 μm. **(b)** SEM image of nanowires (pixel 24) with radii of 175 nm, 2.8 μm height and 800 nm pitch sitting on mesa with height of 5 μm. Scale bar is 10 μm. Inset: zoom-in of nanowires with 1 μm scale bar. **(c)** SEM image of nanowires (pixel 24) embedded in SU-8 epoxy layer. Scale bar is 1 μm. **(d)** False colored

SEM image of pixel 24 (NW radius 175 nm). Color code of Figure 2b is again employed, i.e. light green is SU-8, red is p+ Si NW tips covered with ITO, yellow is ITO and brown/gold is Au. Scale bar is 50 μm. Inset shows magnified view of nanowire array, showing ITO on NW tips (red), ITO on SU-8 (yellow) and Au (brown/gold), with 5 μm scale bar.

OPTICAL PROPERTIES OF DEVICES (SIMULATION AND EXPERIMENT)

We next investigate the optical properties of our device. We use electromagnetic simulations to predict the absorption spectra of the pixels as a function of NW radius. These results are then compared to those obtained by experiment. We begin by describing our simulation results. These are obtained with the finite-difference time domain (FDTD) method using a commercial package (Lumerical FDTD). The geometric parameters of the modelled structures are chosen to match those of our design as closely as practicable. The NWs are taken to have heights of 2.8 μm and to be formed in square arrays with period 800 nm. The medium surrounding the NWs is taken to have a refractive index that matches that of SU-8. This is assumed to extend to the tops of the NWs. The simulations include the ITO (90 nm thick) on the tops of the nanowires. The ITO is assumed to sit on the tops of the NWs. The refractive indices of the Si and ITO are taken from [29, 30] while the refractive index of SU-8 3005 is taken as that provided by the manufacturer in the datasheet. Simulations are performed with the NW radii swept from 50 to 160 nm with a step size of 5 nm. The results are shown as Fig. 4a and Fig 4b. In these plots, we show the external quantum efficiency (EQE) spectra of the NW photodetectors and of the bottom (planar) photodetectors. These are obtained as follows. We first determine the fractional absorption in the silicon regions that would correspond to the intrinsic (n-) sections of these detectors. This is done by calculating the net power loss in the intrinsic section of the NW photodetector. We similarly calculate the net power loss in the intrinsic section of bottom (planar) photodetector. In this way, we determine the fractional light absorption in the nanowire and bottom photodetectors. Under the assumption that

our detectors have unity (100%) internal quantum efficiency (IQE), this quantity also corresponds to EQE. This is a convenient assumption as it allows us to later quantify the IQE of fabricated devices by comparing the simulated EQE (that assumes 100% IQE) to the measured EQE. Differences between simulation and experiment are thus indicative of the actual IQE achieved in fabricated devices. The simulated EQE spectra are plotted as Fig. 4a and Fig. 4b. It can be seen that the simulated NW EQE spectra exhibit peaks that red-shift as the NW radius is increased (Fig. 4a). As indicated on this plot, these originate from the HE_{12}, HE_{13}, HE_{14} waveguide modes supported by the NWs. These modes are denoted in the plots by green dashed lines that represent guides to the eye. A feature corresponding to the HE_{11} mode also can be seen at longer wavelengths (Fig. 4a), though with substantially smaller absorption (and thus EQE). It can be seen from Fig. 4b that the bottom planar detector has EQE spectra with Fabry-Perot ripple features[28] and with notches (i.e. reduced EQE) at wavelengths corresponding to the absorption peaks in the NWs. In other words, the NWs act as filters for the underlying planar photodetector, as desired.

We first measure the current-voltage (I-V) characteristics of the pixels using a picoammeter (Keithley 6485). We scan the voltage to each pixel from -3.0 to +3.0 V and measure the current. These measurements are performed with and without illumination. The illumination source is a laser driven light source (LDLS, Energetiq EQ-99X) coupled to a monochromator (Princeton Instrument Acton SpectraPro 2150). The light emerging from the monochromator light source is focused onto each pixel with a microscope objective lens (Nikon LU Plan Fluor, 0.30 NA, 10×). In Fig. 4c, we show the I-V characteristic of a typical device. This is for pixel 13, for which the NWs have a nominal (design value) radius of 120 nm. For the I-V characteristic measured under illumination (“light”), the monochromator is set to produce light with a wavelength of 532 nm. The optical power used for the measurement of 4.2 μW, as determined with an optical power meter

(Thorlabs PM100D). The I-V characteristics of Fig. 4c can be understood by noting that the device consists of two diodes connected in series as depicted in Fig. 1b. When the device is not illuminated (Fig. 4c, “dark”), the I-V characteristic can be understood as follows. When negative bias is applied to the device, the NW diode is reverse-biased, while the planar diode is forward biased. Similarly, when positive bias is applied, the NW diode is forward biased, while the planar diode is reverse biased. We next consider the I-V characteristic measured when the device is illuminated (Fig. 4c, “light”). It can be seen that the current minimum occurs when the bias to the device is slightly negative. This indicates that the open circuit voltage for the planar diode is larger than the open circuit voltage of the NW diode for this illumination condition. It can be seen that the current reaches a plateau for applied voltages greater than ~-2.4 V in the negative sense. When this occurs, the NW diode is reverse-biased, while the planar diode is forward-biased. The photocurrent that occurs thus originates from light absorbed within the intrinsic region of the NW diode. It can also be seen that another plateau occurs for applied voltages greater than ~+1.2 V. This corresponds to the NW diode being forward-biased, while the planar diode is reverse-biased. In this situation, the photocurrent that occurs comes from the light absorbed on the intrinsic region of the planar diode. For this pixel at the illumination condition employed, we can see that the photocurrent (which originates from light absorbed in the NWs) is in excess of 400 times greater than the dark current when the bias voltage is -3 V. Similarly, the photocurrent (which originates from light absorbed in the planar diode) is more than 3×10^4 times greater than the dark current when the bias voltage is +3 V.

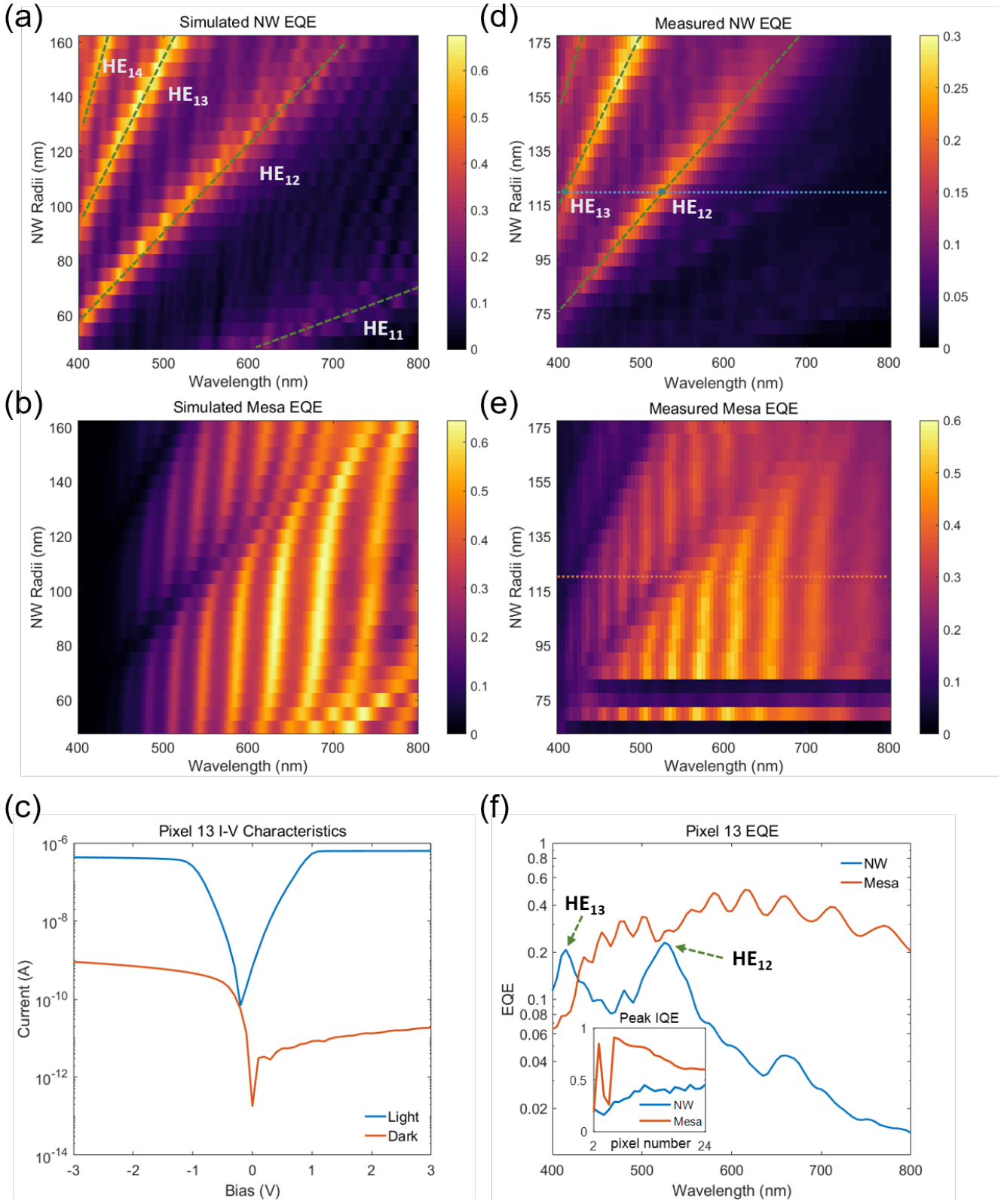


Figure 4. Device simulation and characterization. **(a)** & **(b)** FDTD simulated EQE spectra of nanowire **(a)** and mesa **(b)** photodetectors. Nanowire radii range from 50 -160 nm. **(c)** Current-

voltage characteristics of pixel 13 with nanowire radius of 120 nm with device in the dark (red curve) and with illumination (blue curve). Illumination is monochromatic (wavelength 532 nm) and has power of 4.2 μW. **(d)** & **(e)** Measured EQE spectra of nanowire **(d)** and mesa **(e)** photodetectors of pixels 2-24. Nominal nanowire radii range from 65 to 175 nm. **(f)** External quantum efficiency of pixel 13 (logarithmic scale). Red and blue curves show EQE of mesa and nanowire photodetectors, respectively. Inset shows the peak IQE of nanowire ("NW") and mesa photodetectors from pixels 2-24.

We next characterize the spectral response of the devices on our chip. To do so, we scan the monochromator in wavelength from 400 to 800 nm, with a step size of 5 nm. At each wavelength, we measure the current under reverse (-3 V) and forward (+3 V) biases. After this data has been collected, we use the power meter to measure the optical power illuminating the device at each wavelength. We also measure the dark current under reverse (-3 V) and forward (+3 V) biases. We then find the responsivity (R) spectrum of each pixel by dividing the photocurrent by the optical power incident on the device. Here, the photocurrent is given by the measured current (with illumination) minus the dark current. The responsivity is then converted to EQE ($= R \times hc/(q\lambda)$), where R is the measured photoresponsivity, h is Planck's constant, c is the speed of light in vacuum, q is the electron charge and λ is the wavelength. The results are plotted as Fig. 4d,e,f. It should be noted that pixel 1 containing NWs with (nominal) radii of 60 nm was damaged at the start of the characterization experiment. We therefore show the EQE spectra of pixels 2-24 in Fig 4d and 4e. It can be seen that that the NW EQE spectra (Fig. 4d) exhibit peaks that shift to longer wavelengths as the NW radii are increased. This is consistent with the predictions of simulations (Fig. 4a), thus allowing us to identify the associated waveguide modes. These modes are indicated on Fig. 4d, with green dashed lines added as guides to the eye. It should be noted that the peak positions of the measured EQE are in agreement with the peak positions predicted by simulations for NWs with radii that are 15 nm smaller. It is for this reason that the simulated EQE are for NWs with radii from 50 to 160 nm (Fig. 4a), while the nominal (design) radii of the fabricated NWs are

65 to 175 nm (Fig. 4d, i.e. excluding the damaged pixel 1 with nominal radii 60 nm). From Fig. 4e, it can be seen that the planar (mesa) photodetectors have EQE spectra with Fabry-Perot ripples as expected from simulations (Fig. 4b). They furthermore exhibit notches, at which the EQE is suppressed, at wavelengths corresponding to enhanced absorption in the NWs. It can also be seen from Fig. 4d that the measured NW EQE spectra show an additional peak that is not apparent in the simulations (Fig 4a). This peak is weaker (i.e. has smaller EQE) than the others and is to the right of the HE12 mode in Fig. 4d. This peak can also be seen in Fig. 4f. We attribute the fact that this peak is observed in experiments (Fig. 4b) but not predicted by simulations (Fig. 4a) to the fact that, unlike the simulations of Fig. 4b, in experiments the illumination is not purely at normal incidence. Indeed, this feature is present in simulations of the structure with angled incidence (Supporting Information). The EQE measurement of pixel 13 is shown in Figure 4(f), with the peaks of the NW responsivity corresponding to the intersections between the blue dashed line and green dashed lines in Figure 4(d). These peaks, at which EQE ~ 0.2, correspond to the HE_{12} and HE_{13} modes. Note that the average peak EQE value of the nanowire detectors is 0.21. On the other hand, the simulated average peak EQE values of the nanowire detectors is 0.58. We calculate the peak IQE of nanowires by comparing the measured peak EQE of nanowires to the simulated peak EQE values (which assume unity IQE). The result is shown in the inset of Fig 4f. The mean peak NW IQE of pixels 2-24 is ~38%. This is relatively modest, though higher than our previous work[20]. It is likely mainly due to the silicon crystalline structure being damaged at the surface by the dry etching process. We anticipate that the quantum efficiency could be improved by adding an aluminum oxide passivation layer[31] using atomic layer deposition (ALD) or using alternative nanowire synthesis methods such as metal-assisted chemical etching[32] or VLS growth[23]. From the plot we can also see that nanowires detectors with smaller radii generally have lower EQE values.

Possible reasons include these nanowires being more susceptible to the effects of surface recombination and the ITO being less transparent at shorter wavelengths. The ITO is deposited by RF sputtering. It is known that such films benefit from thermal annealing, which can improve its overall transparency and significantly reduce its resistance[33]. This is not feasible with our process, as the SU-8 epoxy (on which the ITO is supported) cannot withstand temperatures above 200 °C. It may be fruitful in the future to experiment with modifying the ITO sputtering parameters to improve its transmittance at short wavelengths[34].

In Figure 4(e), we show the EQE data of all mesa photodetectors. Pixel 2, 4 and 5 have much lower photoresponse than the others. The reason for this remains unclear. The remaining mesa photodetectors have photoresponse consistent with our expectations from the simulations. Using the same method as that used for the nanowires, the IQE of the mesa detectors (excluding the defective pixels 2,4,5) is estimated to be ~73 %. This is higher than that for the nanowires. From Figure 4(f), the complementary effect of NW absorption can again be seen, with the dips in the mesa EQE occurring at the positions of the peaks in the NW EQE. See Supporting Information for further analysis of the sensitivity of the fabricated photodetectors.

SPECTRAL RECONSTRUCTION

We next demonstrate spectral reconstruction with our chip. To generate test spectra, we take light from our LDLS and pass it through optical filters. The monochromator is bypassed. To generate the “green” spectrum (as it is denoted hereafter), the light is passed through a colored glass filter (Thorlabs FD1G). Similarly, the “red” spectrum is generated by passing the light through a

different colored glass filter (Thorlabs FD1R). We use the same experimental set-up (i.e. microscope objective) as before to focus the light onto the chip, measuring the current from each pixel under forward and reverse biases (i.e. ±3 V). The spectral reconstruction can be formulated as a classic inverse problem. To understand how it is performed, we begin by considering the photocurrent from each photodetector. This can be expressed as follows:

$$I_k = \int_{\lambda_1}^{\lambda_2} R_k(\lambda)P(\lambda) + n_k(\lambda)\,\mathrm{d}\lambda, k = 1,2,\dots,N \quad (1)$$

where $P(\lambda)$ is input spectrum, I_k is the photocurrent of photodetector k, R_k is the responsivity spectrum of photodetector k and n_k is the measurement noise. N is the number of photodetectors. λ_1 and λ_2 are the bounds of the spectrum. After discretization, Eqn (1) can be expressed in vector form as follows:

$$I_k = \boldsymbol{R_k^T}[\lambda]\boldsymbol{P}[\lambda] + n_k, \qquad k = 1,2,\dots,N \quad (2)$$

where $\boldsymbol{R_k^T}[\lambda]$, $\boldsymbol{P}[\lambda]$ are the row and column vector forms of R_k and P_k.

We use the recursive least square algorithm[35] (RLS) to perform linear estimation, i.e. to estimate the input spectrum. The algorithm searches for the estimation $\widetilde{\boldsymbol{P}}[\lambda]$ to minimize a weighted least square error cost function in an iterative fashion. The reconstructed "green" and "red" spectra are shown as Figure 5a and 5b. It can be seen that these are in reasonable agreement with the reference spectra measured directly by a commercial spectrometer (Ocean Optics QEPro). In Fig 5c, photocurrents are shown for the NW and planar (mesa) photodetectors. Measured and estimated photocurrents are shown. The former are the photocurrents we measure in the experiments. The latter are generated as follows. For each photodetector, the estimated photocurrent is given by the integral of the product of the estimated spectrum $\widetilde{\boldsymbol{P}}[\lambda]$ and the previously measured responsivity

spectrum $\boldsymbol{R_k}$ over the wavelength range under consideration. The illumination source for Fig. 5c is the 'red' light source. In the reconstructions, we do not use the results of pixel 1 because as discussed, it is damaged at the beginning of the characterization step. We furthermore do not use pixels 2, 4 and 5, as these have much lower responsivities. The reconstructions are thus performed using data from 40 photodetectors. It can be seen that measured and estimated photocurrents generally match well. The results for the NW device of pixel 3 do not match as well as the other photodetectors. We attribute this to the lower responsivity of this device. We next quantify the performance of our device using the mean square error (MSE) which is defined as follows,

$$MSE = \frac{1}{M}\sum_{k=1}^{M}\left(\widehat{\boldsymbol{P}}[\lambda_k] - \widetilde{\boldsymbol{P}}[\lambda_k]\right)^2, k = 1,2,\dots,M \quad (3)$$

where M is the discretised spectral length, $\widehat{\boldsymbol{P}}[\lambda_k]$ and $\widetilde{\boldsymbol{P}}[\lambda_k]$ are the normalized power spectral density (ground truth, as measured by reference spectrometer) and normalized reconstructed power spectral density, respectively. The MSE values for 'green' and 'red' spectral reconstructions are 0.0146 and 0.0094, respectively. It can be seen that the peak wavelength of each reconstructed spectrum is in very good agreement with the corresponding reference spectrum. The spectral shapes are also in agreement, though with differences such as fine features not being reproduced and spurious peaks at low intensity. We believe that this may be in part due to the modest number of photodetectors (40) we use. We anticipate that the performance could be further improved by increasing the pixel count, i.e. enabling larger number of NW radius and pitch varieties. Our previous simulation work studied this quantitatively[36]. We next test our spectrometer with narrower input spectra. These are generated by the same system that we use to measure responsivity, i.e. with light from laser driven light source coupled to the monochromator. The spectral reconstructions obtained with our spectrometer chip for eight such spectra are shown as

Fig. 5d. Each spectrum consists of a single peak. The wavelengths of these peaks vary from 480 nm to 690 nm with a step size of 30 nm. It can be seen that the spectra reconstructed by our chip match those measured by our commercial spectrometer (QE-Pro). There is complete agreement between our chip and the commercial spectrometer in terms of the wavelength of the peak of each spectrum. The measured linewidths (5-6 nm) are also in good agreement. The reconstructions of Fig. 5d are performed using a method known as least absolute shrinkage and selection operator (Lasso) regression[37]. This algorithm performs L1 regularization, which produces sparse models with few non-zero coefficients. This is better suited to the spectra of Fig. 5d as these are sparse. It may also be fruitful in the future to exploit other approaches to the nanowire pattern design, such as aperiodic nanowire array[38] or radial disorder[39] with the goal of having more variety in the detector responsivity spectra. It would be interesting to consider whether this would lead to more information (as the pixel responses would be increasingly uncorrelated) and thus improve the spectral reconstruction[40]. It would also be interesting to consider extending this concept to other spectral ranges using other materials. For example, Ge[41-43], InP[44], InAsSb[45] have been employed for wavelength-selective absorption in different portions of the infrared (near-infrared to mid-wave infrared).

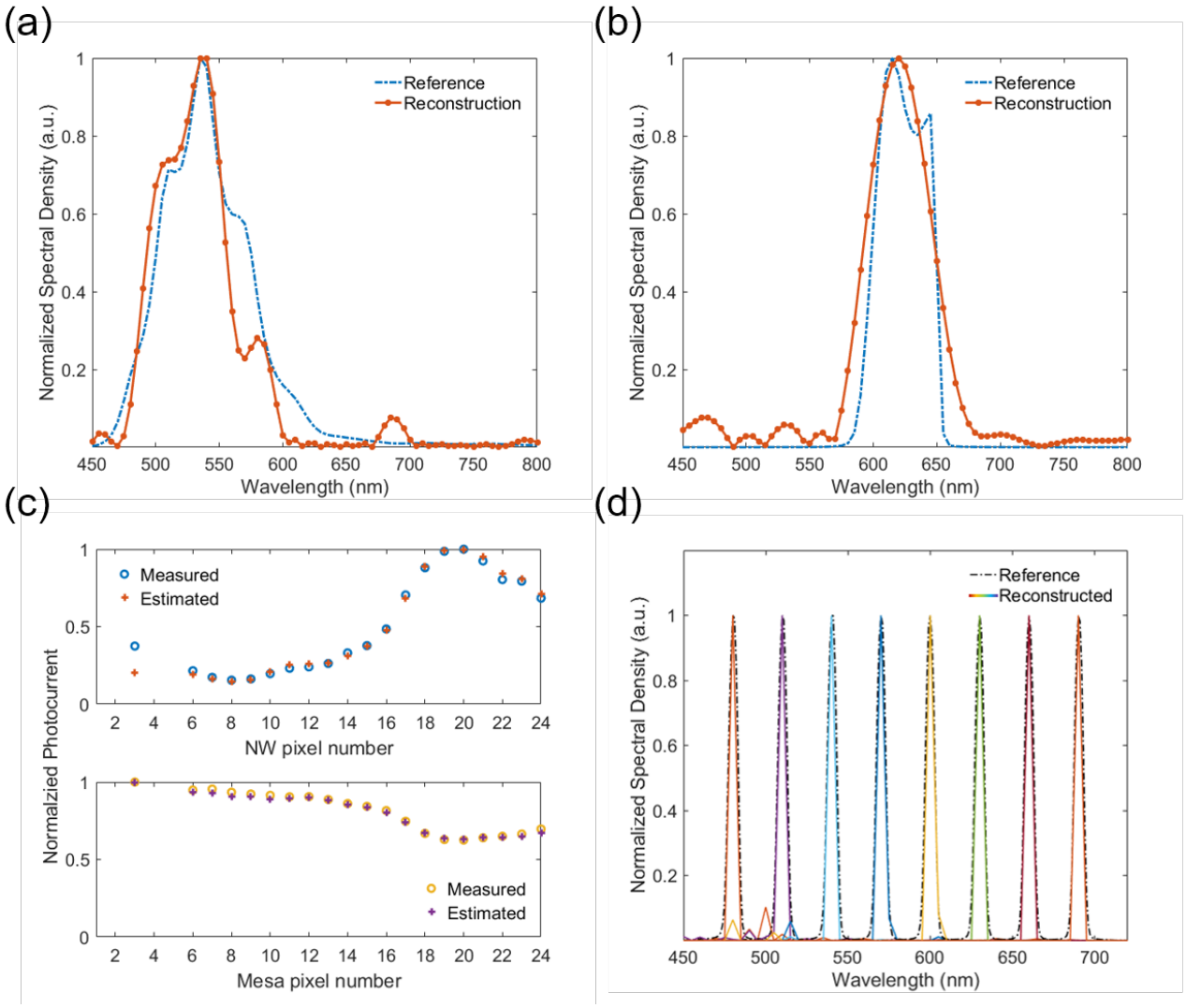


Figure 5. (a)&(b) Measured (blue dash-dot line) and reconstructed (red solid-dot line) spectra of LDLS, filtered through green **(a)** and red **(b)** color glass filters. **(c)** Normalized measured photocurrents (red and purple crosses) and estimated photocurrents (blue and yellow circles) for light filtered through red glass filter. **(d)** Reconstruction results for narrowband spectra. Wavelengths of peaks of spectra range from 480 to 690 nm with 30 nm step size.

CONCLUSION

In summary, we demonstrate a spectrometer comprising an array of vertical silicon nanowire (Si NW) photodetectors formed over an array of planar photodetectors. The top nanowires act as wavelength selective photodetectors and furthermore filter the light transmitted onto the bottom planar photodetectors. We demonstrate an array of 24 such pixels, and employ it as a

microspectrometer, whose design parameters are based on numerical simulations to cover the entire visible spectrum from 400 -800 nm. The responsivities of all photodetectors are defined by the nanowire radii. The fabrication of the device is based on standard Si technology. We characterize the device by measuring its responsivity spectra. The measured average peak IQEs of the fabricated nanowire photodetectors and fabricated mesa photodetectors are ~38% and ~73%, respectively. After the collection of the photocurrent and responsivity data, the spectrum of the light that illuminates the device is reconstructed computationally using the recursive least squares (RLS) algorithm (for broadband spectra) and by lasso regression (for narrowband spectra). Since their demonstration by the vapor liquid solid method some decades ago, silicon nanowires have been employed for a variety of electronic and photonic devices. Here, we demonstrated the use of structurally colored nanowires as a detector-only microspectrometer. We anticipate that our approach will be beneficial for the applications in which the size, weight, power consumption and cost of the spectrometer are the key considerations.

ASSOCIATED CONTENT

Supporting Information

Detailed design parameter sweep. Nanowire etching quality. Incident angle dependence of the absorption spectra. Band diagram of device. Nosie equivalent power of the fabricated photodetectors.

AUTHOR INFORMATION

Corresponding Author

* jiajunm@student.unimelb.edu.au and * kenneth.crozier@unimelb.edu.au

Author Contributions

J.M and K.B.C conceived the experiment, J.M designed and fabricated the devices, J.M and J.J.C performed characterization measurements, J.M implemented the reconstruction algorithms. The manuscript was written through contributions of all authors. All authors have given approval to the final version of the manuscript.

ACKNOWLEDGMENT

This work was supported by the Australian Research Council (LP160100959), by Palette, and by VESKI. This work was performed in part at the Melbourne Centre for Nanofabrication (MCN) in the Victorian Node of the Australian National Fabrication Facility (ANFF).

REFERENCES

1. Lipson, S. G.; Lipson, H.; Tannhauser, D. S., *Optical physics*. 3rd ed.; Cambridge University Press: Cambridge ; New York, NY, USA, 1995; p xviii, 497 p.
2. Wang, S.-W.; Xia, C.; Chen, X.; Lu, W.; Li, M.; Wang, H.; Zheng, W.; Zhang, T. *Optics Letters* **2007,** 32, (6).
3. Correia, J. H.; Bartek, M.; Wolffenbuttel, R. F. *IEEE Transactions on Electron Devices* **2000,** 47, (3), 553-559.
4. Bao, J.; Bawendi, M. G. *Nature* **2015,** 523, (7558), 67-70.
5. Craig, B.; Shrestha, V. R.; Meng, J.; Cadusch, J. J.; Crozier, K. B. *Opt Lett* **2018,** 43, (18), 4481-4484.
6. Ehlermann, J.; Siebels, J.; Fohrmann, S.; Mendach, S. *Applied Physics Letters* **2015,** 106, (10), 101106.
7. Stark, T.; Imboden, M.; Kaya, S.; Mertiri, A.; Chang, J.; Erramilli, S.; Bishop, D. *Acs Photonics* **2015,** 3, (1), 14-19.
8. Zhou, Y.; Wen, Q.; Wen, Z.; Huang, J.; Chang, F. *Journal of Micromechanics and Microengineering* **2017,** 27, (12), 125009.
9. Mao, H. F.; Tripathi, D. K.; Ren, Y.; Silva, K. K. M. B. D.; Martyniuk, M.; Antoszewski, J.; Bumgarner, J.; Dell, J. M.; Faraone, L. *Ieee J Sel Top Quant* **2017,** 23, (2).
10. Vukusic, P.; Sambles, J. R. *Nature* **2003,** 424, (6950), 852-5.
11. Ellenbogen, T.; Seo, K.; Crozier, K. B. *Nano Lett* **2012,** 12, (2), 1026-31.
12. Kumar, K.; Duan, H. G.; Hegde, R. S.; Koh, S. C. W.; Wei, J. N.; Yang, J. K. W. *Nature Nanotechnology* **2012,** 7, (9), 557-561.
13. James, T. D.; Mulvaney, P.; Roberts, A. *Nano Letters* **2016,** 16, (6), 3817-3823.

14. Cao, L. Y.; Fan, P. Y.; Barnard, E. S.; Brown, A. M.; Brongersma, M. L. *Nano Letters* **2010,** 10, (7), 2649-2654.
15. Seo, K.; Wober, M.; Steinvurzel, P.; Schonbrun, E.; Dan, Y. P.; Ellenbogen, T.; Crozier, K. B. *Nano Letters* **2011,** 11, (4), 1851-1856.
16. Kuznetsov, A. I.; Miroshnichenko, A. E.; Fu, Y. H.; Zhang, J. B.; Luk'yanchuk, B. *Scientific Reports* **2012,** 2.
17. Song, W.; Crozier, K. B. In *Observation of visible-wavelength electric and magnetic resonances on silicon nanorods*, CLEO: 2014, San Jose, California, 2014/06/08, 2014; Optical Society of America: San Jose, California, p SW1M.2.
18. Proust, J.; Bedu, F.; Gallas, B.; Ozerov, I.; Bonod, N. *ACS Nano* **2016,** 10, (8), 7761-7.
19. Dong, Z. G.; Ho, J. F.; Yu, Y. F.; Fu, Y. H.; Paniagua-Dominguez, R.; Wang, S. H.; Kuznetsov, A. I.; Yang, J. K. W. *Nano Letters* **2017,** 17, (12), 7620-7628.
20. Park, H.; Dan, Y.; Seo, K.; Yu, Y. J.; Duane, P. K.; Wober, M.; Crozier, K. B. *Nano Lett* **2014,** 14, (4), 1804-9.
21. Park, H.; Crozier, K. B. *Opt Express* **2015,** 23, (6), 7209-16.
22. Cadusch, J. J.; Meng, J.; Craig, B.; Crozier, K. B. *Optica* **2019,** 6, (9), 1171-1177.
23. Wagner, R. S.; Ellis, W. C. *Applied Physics Letters* **1964,** 4, (5), 89-90.
24. Khorasaninejad, M.; Abedzadeh, N.; Walia, J.; Patchett, S.; Saini, S. S. *Nano Letters* **2012,** 12, (8), 4228-4234.
25. Thelander, C.; Agarwal, P.; Brongersma, S.; Eymery, J.; Feiner, L. F.; Forchel, A.; Scheffler, M.; Riess, W.; Ohlsson, B. J.; Gosele, U.; Samuelson, L. *Mater Today* **2006,** 9, (10), 28-35.
26. Yang, I.; Zhang, X.; Zheng, C.; Gao, Q.; Li, Z.; Li, L.; Lockrey, M. N.; Nguyen, H.; Caroff, P.; Etheridge, J.; Tan, H. H.; Jagadish, C.; Wong-Leung, J.; Fu, L. *Acs Nano* **2018,** 12, (10), 10374-10382.
27. Yang, Z.; Albrow-Owen, T.; Cui, H.; Alexander-Webber, J.; Gu, F.; Wang, X.; Wu, T.-C.; Zhuge, M.; Williams, C.; Wang, P.; Zayats, A. V.; Cai, W.; Dai, L.; Hofmann, S.; Overend, M.; Tong, L.; Yang, Q.; Sun, Z.; Hasan, T. *Science* **2019,** 365, (6457), 1017-1020.
28. Park, H.; Crozier, K. B. *ACS Photonics* **2015,** 2, (4), 544-549.
29. Palik, E. D., *Handbook of optical constants of solids*. Academic press: 1998; Vol. 3.
30. König, T. A.; Ledin, P. A.; Kerszulis, J.; Mahmoud, M. A.; El-Sayed, M. A.; Reynolds, J. R.; Tsukruk, V. V. *ACS nano* **2014,** 8, (6), 6182-6192.
31. Wang, W. C.; Lin, C. W.; Chen, H. J.; Chang, C. W.; Huang, J. J.; Yang, M. J.; Tjahjono, B.; Huang, J. J.; Hsu, W. C.; Chen, M. J. *ACS Appl Mater Interfaces* **2013,** 5, (19), 9752-9.
32. Li, X. *Current Opinion in Solid State and Materials Science* **2012,** 16, (2), 71-81.
33. Tuna, O.; Selamet, Y.; Aygun, G.; Ozyuzer, L. *Journal of Physics D: Applied Physics* **2010,** 43, (5).
34. Kurdesau, F.; Khripunov, G.; da Cunha, A. F.; Kaelin, M.; Tiwari, A. N. *Journal of Non-Crystalline Solids* **2006,** 352, (9-20), 1466-1470.
35. Hayes, M. H., *Statistical digital signal processing and modeling*. John Wiley & Sons: 1996.
36. Meng, J.; Li, S.; Crozier, K. B. In *Wavelength-Multiplexed Spectrometer Based on Silicon Nanowire Photodetector Array*, 2017 European Conference on Lasers and Electro-Optics and European Quantum Electronics Conference, Munich, 2017/06/25, 2017; Optical Society of America: Munich, p CK_9_6.
37. Tibshirani, R. *Journal of the Royal Statistical Society: Series B (Methodological)* **1996,** 58, (1), 267-288.

38. Lin, C.; Povinelli, M. L. *Optics express* **2011,** 19, (105), A1148-A1154.
39. Sturmberg, B. C. P.; Dossou, K. B.; Botten, L. C.; Asatryan, A. A.; Poulton, C. G.; McPhedran, R. C.; Martijn de Sterke, C. *Applied Physics Letters* **2012,** 101, (17).
40. Oliver, J.; Lee, W.-B.; Lee, H.-N. *Optics Express* **2013,** 21, (4), 3969-3989.
41. Solanki, A.; Crozier, K. *Applied Physics Letters* **2014,** 105, (19).
42. Solanki, A.; Li, S.; Park, H.; Crozier, K. B. *ACS Photonics* **2017,** 5, (2), 520-527.
43. Li, S. Q.; Solanki, A.; Frigerio, J.; Chrastina, D.; Isella, G.; Zheng, C.; Ahnood, A.; Ganesan, K.; Crozier, K. B. *ACS Photonics* **2019,** 6, (3), 735-742.
44. Ren, D.; Meng, X.; Rong, Z.; Cao, M.; Farrell, A. C.; Somasundaram, S.; Azizur-Rahman, K. M.; Williams, B. S.; Huffaker, D. L. *Nano Lett* **2018,** 18, (12), 7901-7908.
45. Ren, D.; Azizur-Rahman, K. M.; Rong, Z.; Juang, B. C.; Somasundaram, S.; Shahili, M.; Farrell, A. C.; Williams, B. S.; Huffaker, D. L. *Nano Lett* **2019,** 19, (5), 2793-2802.